

Large bandgap quantum anomalous hall insulator in a designer ferromagnet-topological insulator-ferromagnet heterostructure

Qile Li^{1,2,3}, Chi Xuan Trang^{1,2}, Weikang Wu^{4,5}, Jinwoong Hwang⁶, Nikhil Medhekar^{2,3}, Sung-Kwan Mo⁶, Shengyuan A. Yang⁴, Mark T Edmonds^{1,2*}

¹School of Physics and Astronomy, Monash University, Clayton, VIC, Australia.

²ARC Centre for Future Low Energy Electronics Technologies, Monash University, Clayton, VIC, Australia.

³Department of Materials Science and Engineering, Monash University, Clayton, VIC, Australia

⁴Research Laboratory for Quantum Materials, Singapore University of Technology and Design, Singapore 487372, Singapore

⁵ Division of Physics and Applied Physics, School of Physical and Mathematical Sciences, Nanyang Technological University, Singapore 637371, Singapore

⁶Advanced Light Source, Lawrence Berkeley National Laboratory, Berkeley, CA, USA.

* Corresponding author: mark.edmonds@monash.edu

Abstract - Combining magnetism and nontrivial band topology gives rise to quantum anomalous Hall (QAH) insulators and exotic quantum phases such as the QAH effect where current flows without dissipation along quantized edge states. Inducing magnetic order in topological insulators via proximity to a magnetic material offers a promising pathway towards achieving QAH effect at high temperature for lossless transport applications. One promising architecture involves a sandwich structure comprising two single layers of MnBi₂Te₄ (a 2D ferromagnetic insulator) with ultra-thin Bi₂Te₃ in the middle, and is predicted to yield a robust QAH insulator phase with a bandgap well above thermal energy at room temperature (25 meV). Here we demonstrate the growth of a 1SL MnBi₂Te₄ / 4QL Bi₂Te₃ / 1SL MnBi₂Te₄ heterostructure via molecular beam epitaxy, and probe the electronic structure using angle resolved photoelectron spectroscopy. We observe strong hexagonally warped massive Dirac Fermions and a bandgap of 75 ± 15 meV. The magnetic origin of the gap is confirmed by the observation of broken time reversal symmetry and the exchange-Rashba effect, in excellent agreement with density functional theory calculations. These findings provide insights into magnetic proximity effects in topological insulators, that will move lossless transport in topological insulators towards higher temperature.

Introduction

Three-dimensional (3D) topological insulators (TIs) are materials with non-trivial band topology that are distinct from regular band insulators. Due to strong spin-orbit coupling, band inversion and bulk boundary correspondence, the surfaces of 3D TIs host spin polarised massless Dirac cones that are robust against time reversal symmetric perturbations¹⁻³. By introducing long-range magnetic order in the 3D TI, time reversal symmetry (TRS) can be broken, which manifests as a gap opening in the Dirac cones due to exchange interaction and gives rise to novel phases such as the quantum anomalous Hall (QAH) insulator and axion insulator⁴⁻⁶. A QAH insulator possesses chiral edge states within the band gap, and when the chemical potential is tuned into the magnetic gap a quantised Hall conductance and almost zero longitudinal resistance is observed known as the quantum anomalous Hall effect^{7,8}. Characterised by dissipation-less charge transport and perfect spin polarisation, QAH insulators have potential applications in lossless transport, spintronics and topological quantum computing involving braiding of Majorana Fermions⁹.

To date, the QAH effect has been observed in dilute magnetically doped ultra-thin TIs^{7,8} at 30 mK, and up to 1 K in modulation-doped sandwich heterostructures¹⁰, and most recently in five-layer exfoliated flakes of the intrinsic magnetic topological insulator, MnBi_2Te_4 at 1.4 K¹¹. However, the temperature at which the QAH effect is observed in these systems is well below the size of the magnetic gap and the Curie temperature. This is a result of magnetic disorder¹² and the difficulty in incorporating 3d transition metal magnetic dopants.

Rather than incorporating 3d transition metals into the crystal lattice, a more advantageous strategy may be to place two ferromagnetic materials on the top and bottom surfaces of a 3D TI. This will break TRS for topological surface states (TSS) at the two surfaces *via* magnetic proximity, thereby opening an exchange gap and giving rise to a QAH insulator or axion insulator phase^{13,14} (depending on the thickness of the TI layer). However, inducing sufficient magnetic order to open a sizeable exchange gap *via* proximity effects is challenging due to the undesired influence of the abrupt interface potential as a consequence of lattice mismatch between the magnetic material and TI¹⁵. To date, the only demonstration of QAH effect in a ferromagnetic insulator (FMI) – topological insulator (TI) – ferromagnetic insulator (FMI) heterostructure has been in $(\text{Zn}_{1-x}\text{Cr}_x)\text{Te}-(\text{Bi}_{1-y}\text{Sb}_y)_2\text{Te}_3-(\text{Zn}_{1-x}\text{Cr}_x)\text{Te}$, and did not yield an improvement in the temperature at which QAHE was observed in comparison to dilute magnetically doped 3D TIs¹⁶.

To minimise the interface potential when inducing magnetic order *via* proximity, necessitates the use of ferromagnetic insulators such as CrI₃¹⁷, CrGeTe₃¹⁸ and single-layer MnBi₂Te₄¹⁹ that possess similar chemical and structural compositions to 3D topological insulators. A single layer of the intrinsic magnetic topological insulator MnBi₂Te₄ is particularly promising²⁰. Single-layer MnBi₂Te₄ possesses a band gap exceeding 780 meV²¹, and has long-range ferromagnetic order (arising from the Mn²⁺ ions that contribute a 5 μ_B magnetic moment, with the moments coupled ferromagnetically within each layer) and a Curie temperature of 12 K²⁰. Importantly, it is structurally similar to the well-known 3D TI Bi₂Te₃, with the in-plane lattice constant of MnBi₂Te₄ (0.433 nm)²⁰ almost identical to Bi₂Te₃ (0.438 nm)²². Furthermore, single layer MnBi₂Te₄ and Bi₂Te₃ can be grown with molecular beam epitaxy (MBE)^{21,22} allowing the possibility to engineer new ferromagnet / TI heterostructures. This offers simplicity and control far greater than using 2D exfoliation and heterostructure stacking of different van der Waals materials such as Bi₂Te₃ and CrI₃²³.

The near identical crystal and atomic structures of MnBi₂Te₄ and Bi₂Te₃ means that instead of an abrupt interface potential there is a magnetic extension of the Bi₂Te₃ TSS into the MnBi₂Te₄ magnetic layer as depicted in Fig. 1a. This strong interaction of the TI surface states with the Mn²⁺ ions induces a significant exchange splitting in the TSS of the topological insulator thin film and opens a large gap. This type of magnetic extension was first demonstrated on the top surface of a FMI/TI heterostructure comprising 15 quintuple-layer (QL) Bi₂Se₃ with a single layer of MnBi₂Se₄ on the top surface, which yielded a bandgap \sim 100 meV²⁴. However, with only the top TSS gapped and a 15 QL TI layer, the bottom surface would remain gapless and unlikely to yield the QAH effect. A new theoretical proposal showed that if both the top and bottom TSS of an ultra-thin Bi₂Te₃ film are gapped by MBT layers and the inverted band structure is preserved, chiral spin-polarized edge states and a wide bandgap QAH insulator can be formed.²⁵ In this case, depending on the thickness of the Bi₂Te₃ in the heterostructure the bandgap is predicted to be between 38 meV for 1QL Bi₂Te₃ and 60 meV for 4 or 5 QL Bi₂Te₃²⁵.

In this work, we demonstrate the epitaxial growth of such a heterostructure which comprises 4 QL Bi₂Te₃ sandwiched between two single septuple-layers (SL) of MnBi₂Te₄ ([MnBi₂Te₄]_{1SL}-[Bi₂Te₃]_{4QL}-[MnBi₂Te₄]_{1SL}). For simplicity, for the remainder of the paper, we will refer to this structure as MBT/BT/MBT. We then utilise angle-resolved photoelectron spectroscopy (ARPES) at 8 K, which is below the predicted Curie temperature, $T_c=12$ K of 1 SL MnBi₂Te₄ to measure the electronic band structure and size of the induced exchange gap. We observed strong band anisotropy and large hexagonal warping of the massive Dirac Fermion, with a gap of 75 ± 15 meV, which is well above

room temperature thermal broadening and appears to be a promising avenue towards measuring QAH effect at elevated temperatures.

Results & Discussion

High-quality ultra-thin MnBi_2Te_4 and Bi_2Te_3 films and the MBT/BT/MBT heterostructure were grown using molecular beam epitaxy (MBE) on Si (111)- 7×7 substrates. These growths followed established growth procedures that allow for MnBi_2Te_4 and Bi_2Te_3 to be grown down to single layer thickness^{21,22}. Further details can be found in the Methods section. Figure 1b shows the crystal structure of the MBT/BT/MBT heterostructure, with the magnetic moments from Mn atoms labelled with red arrows. The high quality of the films is confirmed from Reflection High Energy Electron Diffraction (RHEED) patterns shown in Figure S1. The sharp, bright streaks indicate that the film is of uniform thickness and high crystallinity. Angle-integrated core level photoelectron spectroscopy was taken on the MBT/BT/MBT heterostructure at $h\nu=100$ eV shown in Fig. 1c, and shows the expected Mn $3p$, Bi $5d$ and Te $4d$ components. However, two distinct Te $4d$ spin-split components separated by 0.7 eV are observed (represented with green and purple shading). The peak positions of the two Te $4d$ components are consistent with two chemical binding environments, one from 1 SL MnBi_2Te_4 and another from the underlying 4QL Bi_2Te_3 , as these binding energy positions are consistent with core level spectra taken independently on a 1 SL MnBi_2Te_4 film and a 4 QL Bi_2Te_3 film as shown in Fig. S2.

Figure 1d - f show ARPES spectra taken on 1SL MnBi_2Te_4 , 4QL Bi_2Te_3 , and the MBT/BT/MBT heterostructure respectively. Each spectrum is overlaid with the corresponding DFT calculated band structure. For 1SL MBT, only a M-shaped valence band is present below the Fermi level indicating a bandgap greater than 780 meV²¹. For 4QL BT, the n -type doping and band dispersion are consistent with previous reports²² where the Dirac cone with Fermi velocity along ΓM , $v_F = 4.1 \pm 0.5 \times 10^5$ m/s is buried within the valence band and appears gapless within our experimental resolution, which is consistent with DFT that predicts 4 QL BT is gapless.²⁶ Additional high-resolution spectra, and Fermi surface map along with overlaid density functional theory (DFT) data can be found in Fig. S3. In the MBT/BT/MBT heterostructure, the band structure away from the Fermi energy ($>1\text{eV}$) is remarkably similar to that of 4QL BT (see Fig.S4 for the full valence band) while the bands near the Dirac region are noticeably different. As shown in the DFT calculated bands in Fig. 1f, unlike in BT, the Dirac cone on the surface of the heterostructure is elevated above the M-shaped valence band, and the Fermi velocity of the Dirac electron band away from the Dirac region along ΓM increases to $v_F =$

$5.0 \pm 0.5 \times 10^5$ m/s. This is significantly larger than that of 4QL BT ($4.1 \pm 0.5 \times 10^5$ m/s), and comparable to the Fermi velocity of 5 SL MnBi_2Te_4 ²¹. DFT calculated orbital projected band structures in Fig. S5 show that the bands in the MBT/BT/MBT heterostructure near the Dirac region are comprised of *p*-orbitals from Bi and Te atoms, with the Mn *d*-bands lying at much higher binding energy. This confirms that the major role of the Mn^{2+} ions is to modify the crystal potential and produce an effective magnetic field in the out-of-plane direction, with negligible *p-d* hybridisation near the Fermi level.

We now turn our attention to the Dirac region of the MBT/BT/MBT heterostructure to investigate the magnetic coupling of the TI surface state, and whether a gap is opened. Figure 2a shows the raw ARPES spectra of the MBT/BT/MBT thin film taken at $h\nu=40$ eV. Whilst there is some spectral weight near Γ in the Dirac point region that is due to Te-orbital-related matrix elements effects (more prominent between $h\nu=47-60$ eV, see Fig. S6 in SI), the system appears to be gapped. To determine the bandgap accurately, we analyse the energy distribution curves (EDC) around the Γ point. Figure 2b shows an EDC curve extracted at the Γ point in Fig. 2a. There are three distinct peak features, the first is located just below the Fermi level and corresponds to the bulk conduction band (BCB). The second and third peaks occur in the Dirac point regime at 0.21 eV and 0.28 eV. We attribute these two peaks to the Dirac electron band and hole band respectively, with the stronger peak at 0.28 eV attributed to the hole band top because of the higher density of states in the nearly flat band near Γ which we depict schematically in the top right corner in Fig. 2b. This clear peak splitting in the EDC spectra confirms there is a bandgap, and to confirm the size of the bandgap we fit the EDC profile with three individual Lorentzian line shapes. This fitting yields the bottom of the electron band to be 0.205 eV and the top of the hole band to be 0.280 eV, resulting in a band gap of 75 ± 15 meV. In Fig.2c, we present a stacking plot of the EDC curves taken within the k range of $\pm 0.1 \text{ \AA}^{-1}$ around Γ , with the EDC at Γ represented as a black curve. The blue points are peak positions of Dirac bands obtained by fitting these EDC curves with the same method used in Fig. 2b. Figure 2d plots the ARPES spectra, overlaid with the EDC analysis band dispersion from Fig. 2c (red points) and DFT band structure, showing excellent agreement and reproduces the key band dispersion features. Photon energy dependent ARPES spectra between 40-65 eV at 8 K were also analyzed using the EDC peak fitting method to confirm the 2D nature of the heterostructure and that the massive Dirac gap does not change with photon energy. Figure 2e plots bandgap as a function of photon energy, and across all photon energies

the fluctuation of the band gap is within our energy resolution of ± 15 meV, and the Fermi velocity equal to $5.0 \pm 0.5 \times 10^5$ m/s. Confirming the 2D nature of the band gap.

In Figure 3 and 4 we now turn to the anisotropy and band warping in the MBT/BT/MBT heterostructure by fitting to a gapped Dirac band model, which self-consistently reassures the band gap value determined from the EDC analysis described above. In Fig. 3a and b we plot the ARPES constant energy contours and the DFT calculated iso-energy contours respectively and highlight the constant energy contours at E_F (Fig. 3c) and 0.4 eV (Fig. 3d). Overall, the agreement between experiment and theory is excellent. In both cases when approaching the massive Dirac gapped region from the Fermi level there is a clear evolution in the Fermi surface from hexagram to hexagon, that shrinks in the gapped region to a point which corresponds to the bottom of the electron band at ~ 0.2 eV, then at 0.25 eV in the hole band the surface texture evolves back into a hexagram upon moving further into the hole band. The overall warping away from the Massive Dirac region is reminiscent of Bi_2Te_3 ³.

The band anisotropy in the Dirac electron band and the warping strength can be explained and modelled by adopting and modifying the Dirac Hamiltonian model of Bi_2Te_3 proposed by Fu²⁷. We include an energy gap to describe the exchange coupling of the TSS with the exchange field $\Delta_e \sigma_z$, where σ_z is the Pauli matrix from the top and bottom surface MBT SLs:

$$\epsilon(k) = D - \sqrt{(\Delta_e + \lambda k^3 \cos(3\theta))^2 + v_F^2 k^2} \quad (1)$$

where D denotes doping level, Δ_e represents the exchange gap, λ is the warping strength, v_F the asymptotic Fermi velocity at large momenta away from the gapped region, k is the wave vector and θ the polar angle with respect to the ΓK direction.

To examine the hexagonal warping strength, we first fit the band dispersion, blue points in Fig. 2c, of the electron band along Γ -M where $\lambda=0$ to equation (1). From the extracted energy distribution curves (EDC) and momentum distribution curves (MDC) we perform a linear fit of the data away from the gapped region to obtain $v_F = 5.0 \pm 0.5 \times 10^5$ m/s, which also yields a value for the doping, $D=0.28$ eV that corresponds to extrapolating the linear fit to $k=0$. Based on this v_F and D we then set Δ_e as a fitting parameter to yield $\Delta_e=78$ meV. This Δ_e value obtained from fitting to the gapped Dirac model is consistent with the gap value of 75 meV obtained from the EDC fitting method. By fixing Δ_e

and v_F , we now fit the Γ -K direction to determine the hexagonal warping strength, $\lambda=418 \text{ eV} \cdot \text{\AA}^3$, which is almost twice as strong as the strength in Bi_2Te_3 ($\sim 250 \text{ eV} \cdot \text{\AA}^3$ ²⁷). We overlay the extracted data points from EDC peak fitting (circles) and the model (solid line) to the ARPES spectra in Fig. 4a and b for Γ -M and Γ -K respectively, showing excellent agreement. Furthermore, we overlay our model with the Fermi surface data in Fig. 4c and reproduce the key features observed experimentally.

We now proceed to confirm the magnetic origin of the band gap in the MBT/BT/MBT heterostructure by demonstrating the observation of band asymmetry as a consequence of broken TRS known as the exchange-Rashba effect²⁸. The interplay between the hexagonal warping and magnetization in our MBT/BT/MBT heterostructure is also expected to result in a band asymmetry along K' - Γ -K directions. In this case, the hexagonal warping term also introduces a non-zero k -dependent out-of-plane spin texture with eigenvalue of $|s_z|$ reaching maxima at K points and zero at M points in the Brillouin zone. Because the warping term is odd under inversion, similar to Bi_2Te_3 , in MBT/BT/MBT $|s_z|$ at minus K point (K') is opposite to s_z at positive K²⁷. If TRS is preserved, the band dispersion remains the same. However, introducing magnetization perpendicular to the sample surface, the exchange field causes the energy shift in the surface state where the energy of states in the $\Gamma K'$ direction with spin s_z parallel to the field direction is lowered while the energy of state along ΓK is increased. As a result, the band dispersion in the surface state along K' - Γ -K direction is asymmetric but remains symmetric along M' - Γ -M because of vanishing out-of-plane spin s_z . In comparison, the Dirac bands in Bi_2Te_3 thin films and bulk crystals are symmetric about Γ in K' - Γ -K directions^{3,29}.

We look for evidence of this in our ARPES spectrum taken at 8 K and photon energy of 63 eV along M' - Γ -M and K' - Γ -K directions shown in Fig.4a and b respectively. Without further analysis, a strong dichroism is already visible in both spectra. To probe this predicted asymmetry, we plot momentum distribution curves (MDC) taken at 0.1 eV below E_F for both M' - Γ -M and K' - Γ -K directions in Fig. 4d and e. We then fit the MDCs with two Lorentzian line shapes, for M' - Γ -M we obtain $-0.049 \pm 0.01 \text{ \AA}^{-1}$ and $+0.05 \pm 0.01 \text{ \AA}^{-1}$ and a negligible asymmetry of 0.001 \AA^{-1} in Dirac electron band, consistent with the theoretical prediction that along ΓM the Dirac bands are symmetric. The fitting for K' - Γ -K on the other hand reveals the position of the left Dirac electron band to be $-0.058 \pm 0.01 \text{ \AA}^{-1}$ while the right branch position sits at $0.043 \pm 0.01 \text{ \AA}^{-1}$, yielding an asymmetry of 0.015 \AA^{-1} , which is greater than our angular resolution of 0.01 \AA^{-1} . This splitting in k of 0.015 \AA^{-1} and band velocity of $3.3 \text{ eV} \cdot \text{\AA}$, allows us to calculate an exchange field of $\sim 50 \text{ meV}$, which further corroborates our band gap value obtained from the EDC analysis mentioned above. Furthermore, the fitting also demonstrates that the

peak area ratio along $K'-\Gamma-K$ is 2.3, compared with 1.7 along $M'-\Gamma-M$. The linear dichroism in $\Gamma-K$ direction has contributions from both broken mirror symmetry from the polarized synchrotron light electric field and magnetization. In $\Gamma-M$ direction, with out-of-plane spin s_z being almost zero, the dichroism originates largely from the light induced symmetry breaking. Therefore, the increase of 0.6 in the peak area ratio in $\Gamma-K$ can be attributed to the magnetisation i.e. the exchange field couples to different s_z components in left and right branches of Dirac electron band along $\Gamma-K$ direction. These states then enter the initial state in dipole matrix element and result in the dichroism. To further confirm this, we examine the DFT calculated surface atom projected band structure in Fig. 4f and g, which also predicts this dispersion asymmetry. Finally, we can rule out quantum confinement as the origin of the band gap opening because the band dispersion in $K'-\Gamma-K$ would have been symmetric under the preserved TRS. Thus, the band asymmetry we observed confirms the magnetic origin of the band gap.

Conclusion

In conclusion, we have grown a designer FMI/TI/FMI van der Waals heterostructure which is a robust QAH insulator with a bandgap of 75 ± 15 meV. We observe a highly anisotropic massive Dirac Fermion resulting from the exchange-Rashba effect, which confirms the magnetic origin of the band gap due to broken TRS. The realisation of robust band gap in a designer heterostructure provides a crucial step towards QAHE and axion insulator phases at elevated temperatures. It also establishes such designer heterostructures as promising platforms for studying novel topological phases and for high-temperature lossless transport applications. Finally, it is an ideal platform for realising recently predicted resonant photovoltaic effects ³⁰ that require both strong hexagonal warping and broken Kramer degeneracy.

Methods

Thin films of MnBi_2Te_4 , Bi_2Te_3 and MBT/BT/MBT were grown using molecular beam epitaxy (MBE) on *n*-type doped silicon (111) substrates under ultra-high vacuum. The samples were immediately transferred after growth to an interconnected ARPES chamber at HERS Beamline 10.0.1, Advanced Light Source (ALS), Lawrence Berkeley National Laboratory.

MnBi_2Te_4 / Bi_2Te_3 / MnBi_2Te_4 thin film growth on Si (111) substrate

Effusion cells were used to evaporate elemental Bi (99.999%), Te (99.95%) and Mn (99.9%) for growth. The deposition rates were measured with a quartz crystal microbalance before growth to ensure the flux ratio of Te to Bi and Mn is greater than 10:1. The silicon (111) substrate was flash annealed to achieve the 7×7 surface reconstruction observed in Reflective High Energy Electron Diffraction (RHEED). The substrate temperature was then kept at 230 °C during the growth process, as this temperature was determined to yield the highest quality growth based off oscillations in the RHEED intensity indicating layer-by-layer growth. 1SL MnBi_2Te_4 was achieved by first growing 1 QL of Bi_2Te_3 , then a bilayer of MnTe was deposited in order to spontaneously form MnBi_2Te_4 . The 1SL MnBi_2Te_4 was subsequently annealed in Te flux for 5-10 mins to improve crystallinity. Following this, 4QL Bi_2Te_3 was grown, followed by 1SL MnBi_2Te_4 . The sample was then annealed in Te flux for 10 mins at 230°C to improve crystallinity. RHEED taken along the $[11\bar{2}]$ and $[110]$ directions are shown in Fig.S1. The sharp high-intensity streaks in the pattern indicates large area single crystal epitaxial growth.

Angle Resolved Photoelectron Spectroscopy (ARPES) measurements

Our ARPES measurements were performed at Beamline 10.0.1 with linear polarised synchrotron light and data was taken using a Scienta R4000 analyser at temperatures between 8K and 15K. The overall energy resolution is 15 meV. The angular resolution is 0.2° or momentum resolution approximately 0.01 \AA^{-1} for the photoelectron kinetic energies measured.

Density Functional Theory Calculations

The first-principles calculations are based on the density functional theory (DFT), using the projector augmented wave (PAW) method³¹ as implemented in the Vienna ab initio Simulation Package (VASP)^{32,33}. The generalized gradient approximation (GGA) with Perdew-Burke-Ernzerhof (PBE) realization³⁴ were adopted for the exchange-correlation potential. The plane-wave cutoff energy was set to be 400 eV. To account for the correlation effects for Mn 3d-electrons, we used the GGA+U method

introduced by Dudarev et al. ³⁵ and the value of $U_{eff} = U - J$ was chosen as 5.34 eV which was adopted from the work of Otkov et al ²⁵. The van der Waals (vdW) corrections have been taken into account by making use of the DFT-D3 approaches ³⁶.

The structure models for $(\text{Bi}_2\text{Te}_3)_4$ and $(\text{MnBi}_2\text{Te}_4)/(\text{Bi}_2\text{Te}_3)_{n=3}/(\text{MnBi}_2\text{Te}_4)$ heterostructures were constructed by stacking the Bi_2Te_3 quintuple layers or MnBi_2Te_4 septuple layers in the order of ABC sequence. For the $(\text{MnBi}_2\text{Te}_4)/(\text{Bi}_2\text{Te}_3)_{n=3}/(\text{MnBi}_2\text{Te}_4)$ heterostructures, the inversion symmetry is preserved. A vacuum layer of 20 Å thickness is added to avoid artificial interactions between periodic images. The in-plane lattice parameters of these slab structures were fixed to the experimental value of Bi_2Te_3 , which is 4.3835 Å ³⁷. The Brillouin zone was sampled by the k-grid with a spacing of $2\pi \times 0.02\text{Å}^{-1}$ within a Γ -centered sampling scheme for structural optimization and electronic structure calculations. Spin-orbit coupling was considered when performing the structural optimization. The energy and force convergence criteria were set to be 10^{-6} eV and 10^{-2} eV/Å, respectively. The surface-resolved band structures were plotted using PyProcar ³⁸. From the DFT results, we constructed the maximally localized Wannier functions (MLWFs) for Mn-d, Bi-p and Te-p orbitals using WANNIER90 ³⁹⁻⁴¹ [11-13] and the iso-energy spectrum was plotted by means of WannierTools ⁴².

Acknowledgements

M.T.E. was supported by ARC DECRA fellowship DE160101157. M.T.E., C.X.T., Q.L. and N. M., acknowledge funding support from ARC Centre for Future Low Energy Electronics Technologies (FLEET) CE170100039. M.T.E., Q. L., C.X.T. acknowledge travel funding provided by the International Synchrotron Access Program (ISAP) managed by the Australian Synchrotron, part of ANSTO, and funded by the Australian Government. This research used resources of the Advanced Light Source, which is a DOE Office of Science User Facility under contract no. DE-AC02-05CH11231. S. A. Y. acknowledges funding from Singapore Ministry of Education AcRF Tier 2 (Grant MOE2019-T2-1-001).

Author contributions M.T.E. devised the experiments. Q. L. analysed the data with assistance from M. T. T. Q. L., C. X. T., performed the MBE growth at Monash University. Q. L., C. X. T., performed the MBE growth and ARPES measurements at the ALS with the support from J.H. and S.-K.M. The DFT calculations were performed by W. W., and S. A. Y.Y. Q. L., and M.T.E. composed the manuscript. All authors read and contributed feedback to the manuscript. We acknowledge Michael Fuhrer for fruitful discussions.

Competing interests The authors declare no competing interests.

FIGURES

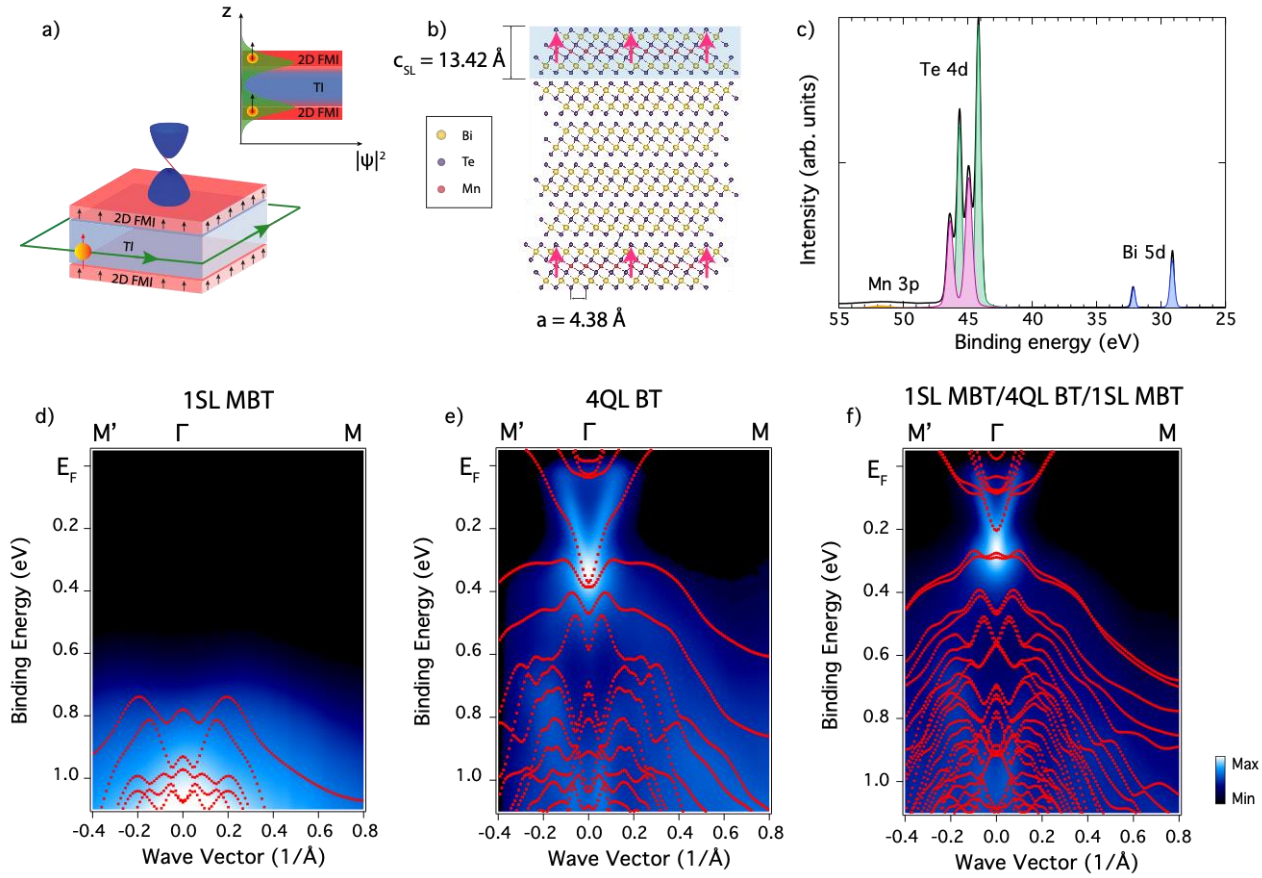


Figure 1 A designer ferromagnetic insulator – topological insulator heterostructure, 1SL MBT / QL BT / 1SL MBT. a) A schematic showing the realisation of the magnetic extension effect in the ferromagnetic insulator (FMI) – topological insulator (TI) heterostructure. Top right corner: wave functions of topological surface state (TSS) (green shaded curve) penetrate into the 2D FMI because of minimal lattice mismatch at the interface, resulting in a QAH insulator with chiral edge modes. b) Crystal structure of 4 quintuple layer (QL) Bi_2Te_3 (BT) sandwiched between two 1 septuple layers (SL) MnBi_2Te_4 (MBT) with the lattice constants labelled, magnetic moments on Mn^{2+} marked by red arrows. The shadowed block indicates 1SL MnBi_2Te_4 . c) Angle-integrated core level photoelectron spectroscopy measurement taken on the MBT/BT/MBT heterostructure at $h\nu = 100 \text{ eV}$, showing the characteristic Mn 3p, Bi 5d and Te 4d peaks. d)- f) ARPES spectra overlaid with DFT calculations along Γ -M direction for 1SL MnBi_2Te_4 , 4QL Bi_2Te_3 and 1SL MBT/ 4QL BT/ 1SL MBT respectively.

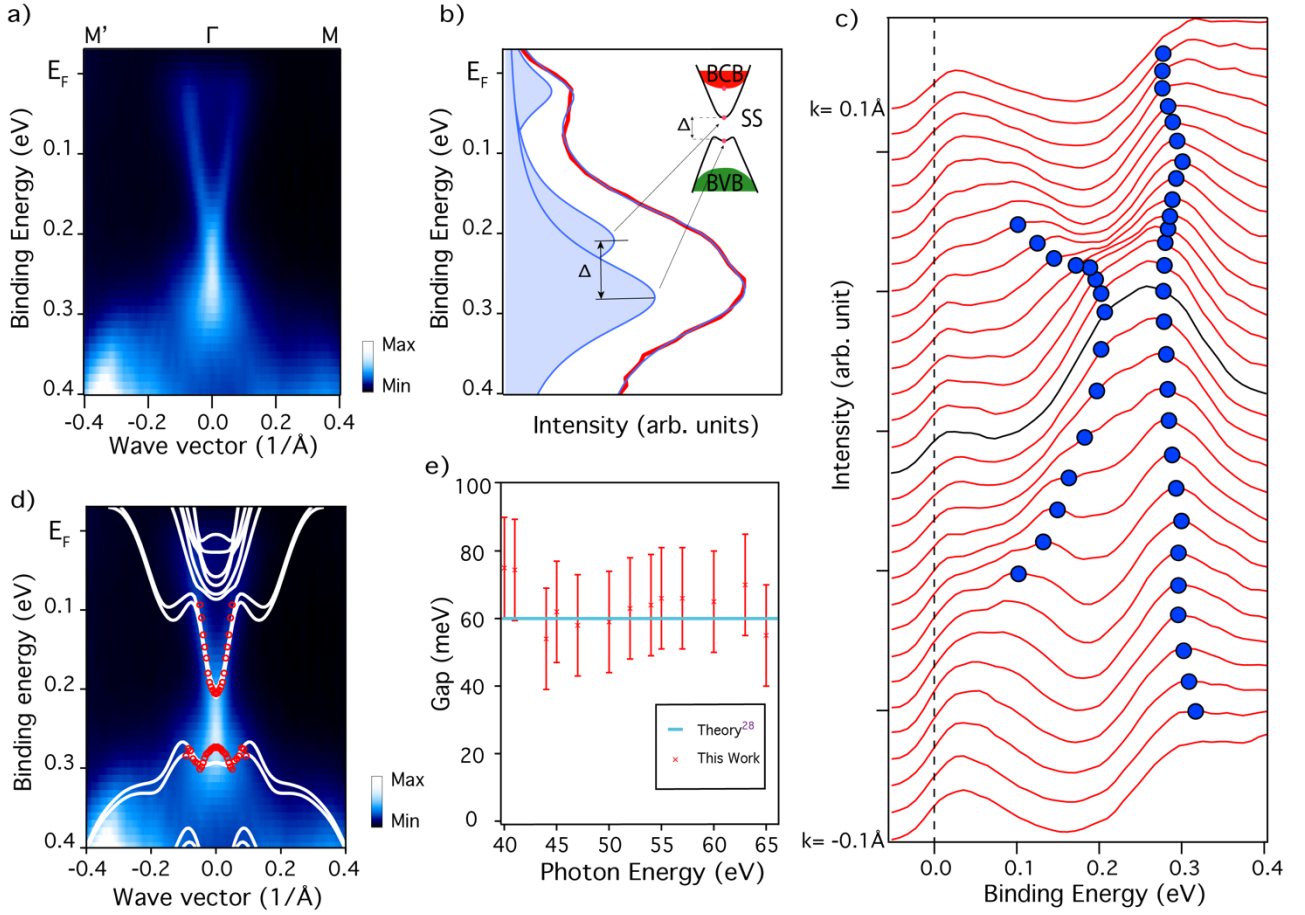


Figure 2 Band gap analysis of MBT/BT/MBT heterostructure and its photon energy dependence. a) ARPES spectra taken on MBT/BT/MBT at $h\nu=40$ eV at 8K with p -polarised light. b) EDC curve (red solid line) at the Γ point, with the fitted curve plotted as blue solid line. The shaded blue peaks represent individual Lorentzian peaks that correspond to the Dirac electron band, hole band and bulk conduction band (BCB). The separation of the hole band and Dirac electron band corresponds to a band gap, $\Delta=75 \pm 15$ meV. c) Stack plot of EDC curves taken within the wave vector range $\pm 0.1 \text{ \AA}^{-1}$. The EDC curve at Γ is highlighted in black and the Blue points are the peak positions obtained from EDC peak fitting analysis. The black dashed line marks the position of the Fermi edge. d) Same ARPES spectrum as in a) but overlaid with DFT calculated bands (white curves) and EDC analysis peaks (red open circles), showing excellent agreement. e) Band gap obtained from EDC analysis as a function of photon energy, the overall band gap value is consistent with the DFT theory plotted as a horizontal blue line.²⁵ An average band gap of 64 ± 15 meV has been obtained from e).

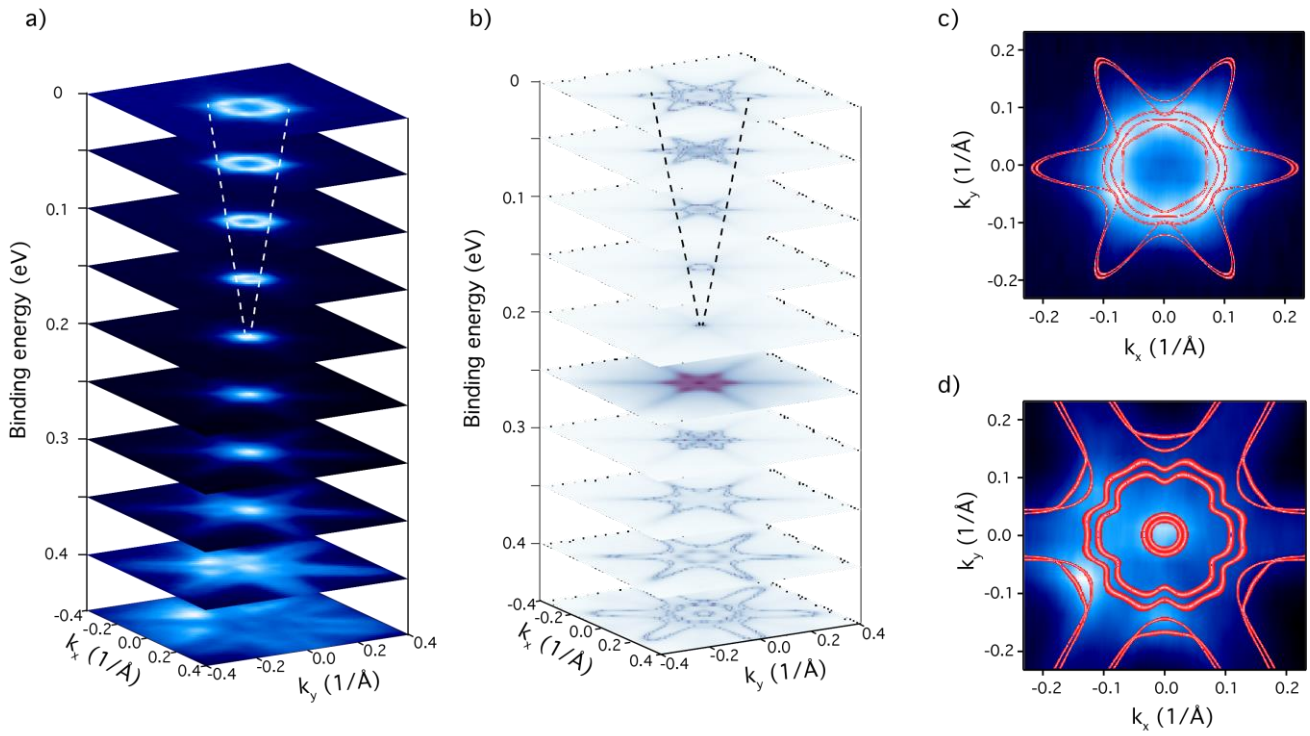


Figure 3 Strong hexagonal warping in the MBT/BT/MBT heterostructure. a) Iso-energy scans taken on MBT/BT/MBT across the gap region between the Fermi level and 0.4 eV. b) DFT calculated iso-energy scans in the same energy range showing excellent agreement. The dashed lines of the Dirac electron band are a guide to the eye. c) Fermi surface (FS) and d) iso-energy cut at 0.4 eV binding energy overlaid with DFT calculated contours in red. The angular intensity distribution shows three-fold symmetry which agrees with the FS calculated by DFT.

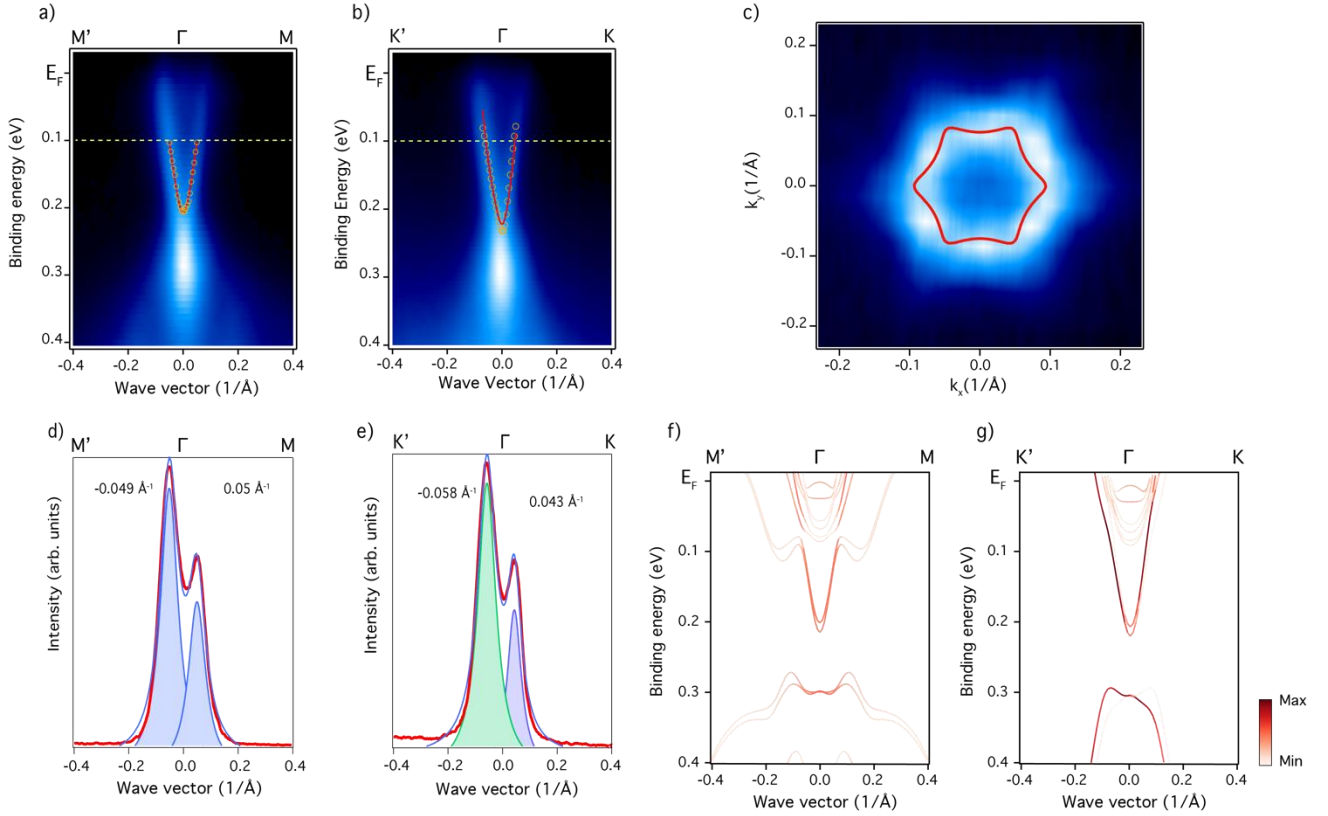


Figure 4 Demonstration of time-reversal symmetry breaking and the exchange Rashba effect. a) ARPES spectrum taken along $M'-\Gamma-M$ direction at 63 eV photon energy, 8K with p -polarised light. The band is symmetric about Γ due to the preserved mirror symmetry and vanishing s_z along ΓM direction. b) ARPES spectrum taken along $K'-\Gamma-K$ at 63eV photon energy, 8K with p -polarised light. c) The Fermi surface scan overlaid with the contour from the model. d) and (e) represent momentum distribution curves (MDC) taken at 0.1eV binding energy from a) and b) (yellow dashed line) respectively and are fitted with two Lorentzian peaks for comparison. A clear asymmetry is observed for $K'-\Gamma-K$ after careful calibration of the Γ point. f) and g) DFT calculated top surface atom projected band structure along $M'-\Gamma-M$ (symmetric) and $K'-\Gamma-K$ (asymmetric) respectively.

Reference

- (1) Fu, L.; Kane, C. L.; Mele, E. J. Topological Insulators in Three Dimensions. *Physical Review Letters* **2007**, *98*.
- (2) Hasan, M. Z.; Kane, C. L. Colloquium: Topological Insulators. *Reviews of Modern Physics* **2010**, *82*, 3045–3067.
- (3) Chen, Y. L.; Analytis, J. G.; Chu, J.-H. ; Liu, Z. K.; Mo, S.-K. ; Qi, X. L.; Zhang, H. J.; Lu, D. H.; Dai, X.; Fang, Z.; *et al.* Experimental Realization of a Three-Dimensional Topological Insulator, Bi₂Te₃. *Science* **2009**, *325*, 178–181.
- (4) Chen, Y. L.; Chu, J. - H.; Analytis, J. G.; Liu, Z. K.; Igarashi, K.; Kuo, H. - H.; Qi, X. L.; Mo, S. K.; Moore, R. G.; Lu, D. H.; *et al.* Massive Dirac Fermion on the Surface of a Magnetically Doped Topological Insulator. *Science* **2010**, *329*, 659–662.
- (5) Rienks, E. D. L.; Wimmer, S.; Sánchez-Barriga, J.; Caha, O.; Mandal, P. S.; Růžička, J.; Ney, A.; Steiner, H.; Volobuev, V. V.; Groiss, H.; *et al.* Large Magnetic Gap at the Dirac Point in Bi₂Te₃/MnBi₂Te₄ Heterostructures. *Nature* **2019**, *576*, 423–428.
- (6) Liu, C.; Wang, Y.; Li, H.; Wu, Y.; Li, Y.; Li, J.; He, K.; Xu, Y.; Zhang, J.; Wang, Y. Robust Axion Insulator and Chern Insulator Phases in a Two-Dimensional Antiferromagnetic Topological Insulator. *Nature Materials* **2020**, *19*, 522–527.
- (7) Chang, C.-Z.; Zhang, J.; Feng, X.; Shen, J.; Zhang, Z.; Guo, M.; Li, K.; Ou, Y.; Wei, P.; Wang, L.-L.; *et al.* Experimental Observation of the Quantum Anomalous Hall Effect in a Magnetic Topological Insulator. *Science* **2013**, *340*, 167–170.
- (8) Chang, C.-Z.; Zhao, W.; Kim, D. Y.; Zhang, H.; Assaf, B. A.; Heiman, D.; Zhang, S.-C.; Liu, C.; Chan, M. H. W.; Moodera, J. S. High-Precision Realization of Robust Quantum Anomalous Hall State in a Hard Ferromagnetic Topological Insulator. *Nature Materials* **2015**, *14*, 473–477.
- (9) He, Q. L.; Pan, L.; Stern, A. L.; Burks, E. C.; Che, X.; Yin, G.; Wang, J.; Lian, B.; Zhou, Q.; Choi, E. S.; *et al.* Chiral Majorana Fermion Modes in a Quantum Anomalous Hall Insulator–Superconductor Structure. *Science* **2017**, *357*, 294–299.
- (10) Mogi, M.; Yoshimi, R.; Tsukazaki, A.; Yasuda, K.; Kozuka, Y.; Takahashi, K. S.; Kawasaki, M.; Tokura, Y. Magnetic Modulation Doping in Topological Insulators toward Higher-Temperature Quantum Anomalous Hall Effect. *Applied Physics Letters* **2015**, *107*, 182401.
- (11) Deng, Y.; Yu, Y.; Shi, M. Z.; Guo, Z.; Xu, Z.; Wang, J.; Chen, X. H.; Zhang, Y. Quantum Anomalous Hall Effect in Intrinsic Magnetic Topological Insulator MnBi₂Te₄. *Science* **2020**, *367*, 895–900.
- (12) Lee, I.; Kim, C. K.; Lee, J.; Billinge, S. J. L.; Zhong, R.; Schneeloch, J. A.; Liu, T.; Valla, T.;

- Tranquada, J. M.; Gu, G.; *et al.* Imaging Dirac-Mass Disorder from Magnetic Dopant Atoms in the Ferromagnetic Topological Insulator $\text{Cr}_x(\text{Bi}_{0.1}\text{Sb}_{0.9})_2\text{-XTe}_3$. *Proceedings of the National Academy of Sciences* **2015**, *112*, 1316–1321.
- (13) Chong, S. K.; Han, K. B.; Nagaoka, A.; Tsuchikawa, R.; Liu, R.; Liu, H.; Vardeny, Z. V.; Pesin, D. A.; Lee, C.; Sparks, T. D.; *et al.* Topological Insulator-Based van Der Waals Heterostructures for Effective Control of Massless and Massive Dirac Fermions. *Nano Letters* **2018**, *18*, 8047–8053.
- (14) Yao, X.; Gao, B.; Han, M.-G.; Jain, D.; Moon, J.; Kim, J. W.; Zhu, Y.; Cheong, S.-W.; Oh, S. Record High-Proximity-Induced Anomalous Hall Effect in $(\text{Bi}_x\text{Sb}_{1-x})_2\text{Te}_3$ Thin Film Grown on CrGeTe_3 Substrate. *Nano Letters* **2019**, *19*, 4567–4573.
- (15) Katmis, F.; Lauter, V.; Nogueira, F. S.; Assaf, B. A.; Jamer, M. E.; Wei, P.; Satpati, B.; Freeland, J. W.; Eremin, I.; Heiman, D.; *et al.* A High-Temperature Ferromagnetic Topological Insulating Phase by Proximity Coupling. *Nature* **2016**, *533*, 513–516.
- (16) Watanabe, R.; Yoshimi, R.; Kawamura, M.; Mogi, M.; Tsukazaki, A.; Yu, X. Z.; Nakajima, K.; Takahashi, K. S.; Kawasaki, M.; Tokura, Y. Quantum Anomalous Hall Effect Driven by Magnetic Proximity Coupling in All-Telluride Based Heterostructure. *Applied Physics Letters* **2019**, *115*, 102403.
- (17) Webster, L.; Yan, J.-A. Strain-Tunable Magnetic Anisotropy in Monolayer CrCl_3 , CrBr_3 , and CrI_3 . *Physical Review B* **2018**, *98*.
- (18) Gong, C.; Li, L.; Li, Z.; Ji, H.; Stern, A.; Xia, Y.; Cao, T.; Bao, W.; Wang, C.; Wang, Y.; *et al.* Discovery of Intrinsic Ferromagnetism in Two-Dimensional van Der Waals Crystals. *Nature* **2017**, *546*, 265–269.
- (19) Li, Y.; Jiang, Z.; Li, J.; Xu, S.; Duan, W. Magnetic Anisotropy of the Two-Dimensional Ferromagnetic Insulator MnBi_2Te_4 . *Physical Review B* **2019**, *100*.
- (20) Otrokov, M. M.; Rusinov, I. P.; Blanco-Rey, M.; Hoffmann, M.; Vyazovskaya, A. Yu.; Ereemeev, S. V.; Ernst, A.; Echenique, P. M.; Arnau, A.; Chulkov, E. V. Unique Thickness-Dependent Properties of the van Der Waals Interlayer Antiferromagnet MnBi_2Te_4 Films. *Physical Review Letters* **2019**, *122*.
- (21) Trang, C. X.; Li, Q.; Yin, Y.; Hwang, J.; Akhgar, G.; Di Bernardo, I.; Grubišić-Čabo, A.; Tadich, A.; Fuhrer, M. S.; Mo, S.-K.; *et al.* Crossover from 2D Ferromagnetic Insulator to Wide Bandgap Quantum Anomalous Hall Insulator in Ultra-Thin MnBi_2Te_4 . *arXiv:2009.06175 [cond-mat]* **2020**.
- (22) Li, Y.-Y.; Wang, G.; Zhu, X.-G.; Liu, M.-H.; Ye, C.; Chen, X.; Wang, Y.-Y.; He, K.; Wang,

- L.-L.; Ma, X.-C.; *et al.* Intrinsic Topological Insulator Bi₂Te₃ Thin Films on Si and Their Thickness Limit. *Advanced Materials* **2010**, *22*, 4002–4007.
- (23) Hou, Y.; Kim, J.; Wu, R. Magnetizing Topological Surface States of Bi₂Se₃ with a CrI₃ Monolayer. *Science Advances* **2019**, *5*, eaaw1874.
- (24) Hirahara, T.; Ereemeev, S. V.; Shirasawa, T.; Okuyama, Y.; Kubo, T.; Nakanishi, R.; Akiyama, R.; Takayama, A.; Hajiri, T.; Ideta, S.; *et al.* Large-Gap Magnetic Topological Heterostructure Formed by Subsurface Incorporation of a Ferromagnetic Layer. *Nano Letters* **2017**, *17*, 3493–3500.
- (25) Otrokov, M. M.; Menshchikova, T. V.; Vergniory, M. G.; Rusinov, I. P.; Yu Vyazovskaya, A.; Koroteev, Y. M.; Bihlmayer, G.; Ernst, A.; Echenique, P. M.; Arnau, A.; *et al.* Highly-Ordered Wide Bandgap Materials for Quantized Anomalous Hall and Magnetoelectric Effects. *2D Materials* **2017**, *4*, 025082.
- (26) Yazyev, O. V.; Moore, J. E.; Louie, S. G. Spin Polarization and Transport of Surface States in the Topological Insulators Bi₂Se₃ and Bi₂Te₃ from First Principles. *Physical Review Letters* **2010**, *105*.
- (27) Fu, L. Hexagonal Warping Effects in the Surface States of the Topological Insulator Bi₂Te₃. *Physical Review Letters* **2009**, *103*.
- (28) Otrokov, M. M.; Klimovskikh, I. I.; Bentmann, H.; Estyunin, D.; Zeugner, A.; Aliev, Z. S.; Gaß, S.; Wolter, A. U. B.; Koroleva, A. V.; Shikin, A. M.; *et al.* Prediction and Observation of an Antiferromagnetic Topological Insulator. *Nature* **2019**, *576*, 416–422.
- (29) Wang, G.; Zhu, X.-G.; Sun, Y.-Y.; Li, Y.-Y.; Zhang, T.; Wen, J.; Chen, X.; He, K.; Wang, L.-L.; Ma, X.-C.; *et al.* Topological Insulator Thin Films of Bi₂Te₃ with Controlled Electronic Structure. *Advanced Materials* **2011**, *23*, 2929–2932.
- (30) Bhalla, P.; MacDonald, A. H.; Culcer, D. Resonant Photovoltaic Effect in Doped Magnetic Semiconductors. *Physical Review Letters* **2020**, *124*.
- (31) Blöchl, P. E. Projector Augmented-Wave Method. *Physical Review B* **1994**, *50*, 17953–17979.
- (32) Kresse, G.; Hafner, J. Ab Initio Molecular-Dynamics Simulation of the Liquid-Metal–Amorphous-Semiconductor Transition in Germanium. *Physical Review B* **1994**, *49*, 14251–14269.
- (33) Kresse, G.; Furthmüller, J. Efficient Iterative Schemes For Ab Initio Total-Energy Calculations Using a Plane-Wave Basis Set. *Physical Review B* **1996**, *54*, 11169–11186.
- (34) Perdew, J. P.; Burke, K.; Ernzerhof, M. Generalized Gradient Approximation Made Simple. *Physical Review Letters* **1996**, *77*, 3865–3868.

- (35) Dudarev, S. L.; Botton, G. A.; Savrasov, S. Y.; Humphreys, C. J.; Sutton, A. P. Electron-Energy-Loss Spectra and the Structural Stability of Nickel Oxide: An LSDA+U Study. *Physical Review B* **1998**, *57*, 1505–1509.
- (36) Grimme, S.; Antony, J.; Ehrlich, S.; Krieg, H. A Consistent and Accurate Ab Initio Parametrization of Density Functional Dispersion Correction (DFT-D) for the 94 Elements H-Pu. *The Journal of Chemical Physics* **2010**, *132*, 154104.
- (37) Francombe, M. H. Structure-Cell Data and Expansion Coefficients of Bismuth Telluride. *British Journal of Applied Physics* **1958**, *9*, 415–417.
- (38) Herath, U.; Tavadze, P.; He, X.; Bousquet, E.; Singh, S.; Muñoz, F.; Romero, A. H. PyProcar: A Python Library for Electronic Structure Pre/Post-Processing. *Computer Physics Communications* **2020**, *251*, 107080.
- (39) Marzari, N.; Vanderbilt, D. Maximally Localized Generalized Wannier Functions for Composite Energy Bands. *Physical Review B* **1997**, *56*, 12847–12865.
- (40) Souza, I.; Marzari, N.; Vanderbilt, D. Maximally Localized Wannier Functions for Entangled Energy Bands. *Physical Review B* **2001**, *65*.
- (41) Mostofi, A. A.; Yates, J. R.; Lee, Y.-S.; Souza, I.; Vanderbilt, D.; Marzari, N. Wannier90: A Tool for Obtaining Maximally-Localised Wannier Functions. *Computer Physics Communications* **2008**, *178*, 685–699.
- (42) Wu, Q.; Zhang, S.; Song, H.-F.; Troyer, M.; Soluyanov, A. A. WannierTools: An Open-Source Software Package for Novel Topological Materials. *Computer Physics Communications* **2018**, *224*, 405–416.

Supplementary Information

Large bandgap quantum Anomalous hall insulator in a designer ferromagnet-topological insulator-ferromagnet heterostructure

Qile Li^{1,2,3}, Chi Xuan Trang^{1,2}, Weikang Wu^{4,5}, Jinwoong Hwang⁶, Nikhil Medhekar^{2,3}, Sung-Kwan Mo⁶, Shengyuan A. Yang⁴, Mark T Edmonds^{1,2*}

¹School of Physics and Astronomy, Monash University, Clayton, VIC, Australia.

²ARC Centre for Future Low Energy Electronics Technologies, Monash University, Clayton, VIC, Australia.

³Department of Materials Science and Engineering, Monash University, Clayton, VIC, Australia

⁴Research Laboratory for Quantum Materials, Singapore University of Technology and Design, Singapore 487372, Singapore

⁵ Division of Physics and Applied Physics, School of Physical and Mathematical Sciences, Nanyang Technological University, Singapore 637371, Singapore

⁶Advanced Light Source, Lawrence Berkeley National Laboratory, Berkeley, CA, USA.

* Corresponding author: mark.edmonds@monash.edu

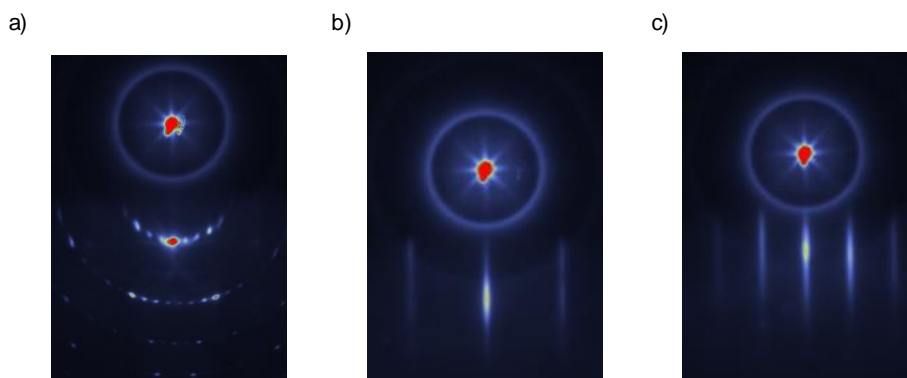


Figure S1 Reflective High Energy Electron Diffraction (RHEED) pattern obtained at 15kV, 1.5A. a) Clean Si (111) substrate showing 7x7 surface reconstruction before growth. b) RHEED of MBT/BT/MBT heterostructure taken after growth along $[11\bar{2}]$ direction and c) taken along $[110]$ direction. The sharp high intensity streaks in the patterns indicate large area of single-crystal epitaxial thin films.

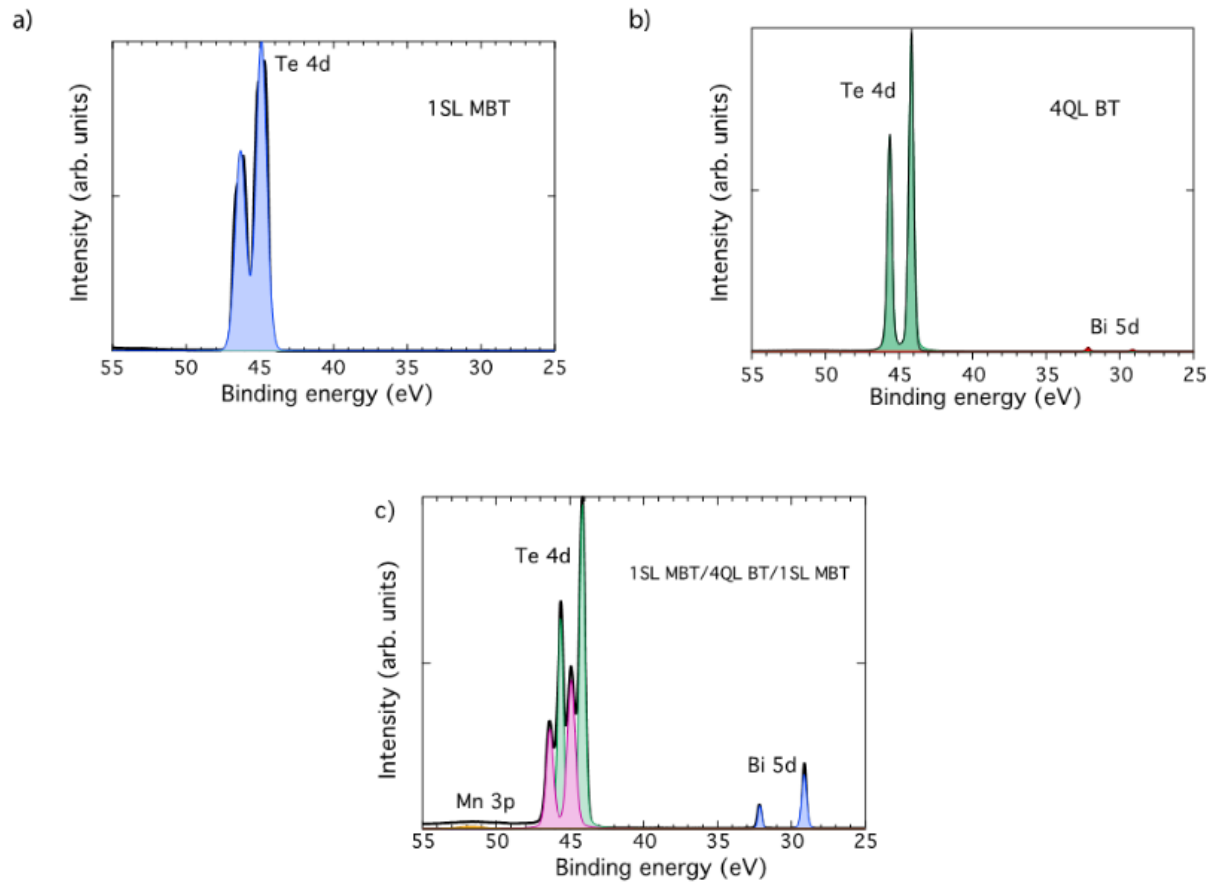


Figure S2 X-ray Photoelectron Spectroscopy (Angle-integrated core level photoelectron spectroscopy) data taken at 100 eV photon energy to characterise the shallow Te 4d core levels of a) 1SL MBT on Si (111) substrate, b) 4QL BT on Si (111) substrate and c) MBT/BT/MBT heterostructure. The core level peaks are fit with Voigt line shapes with Shirley background. The positions of Te 4d doublet in a) 1SL MBT coincides with the 4d Te doublets in c) and positions of Te 4d peaks in 4QL BT coincides with the other doublet at lower binding energy. The presence of two Te 4d doublets can be attributed to Te in two bonding environments from MBT and underlying BT layer.

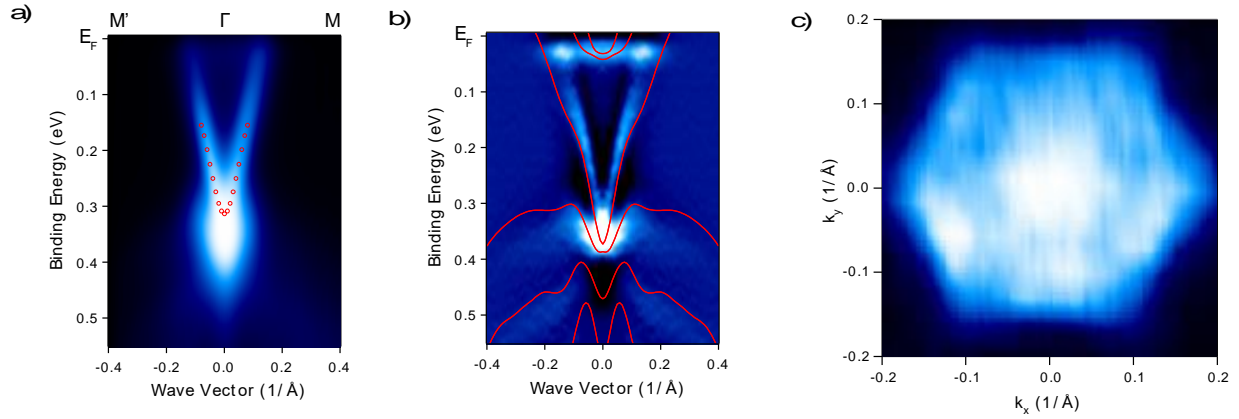


Figure S3 High resolution scan of 4QL BT near the gap region. a) Original ARPES spectrum taken at 54eV photon energy with P-polarised light overlaid with Lorentzian peak positions as red points from EDC analysis. Fitting to these data points yields asymptotic velocity of $2.7 \text{ eV} \cdot \text{Å}$. b) Second derivative enhanced spectrum overlaid with DFT band structure. c) Fermi surface of BT, showing different overall shape from the MBT/BT/MBT heterostructure with intensity from bulk conduction band in the centre but with similar hexagonal symmetry.

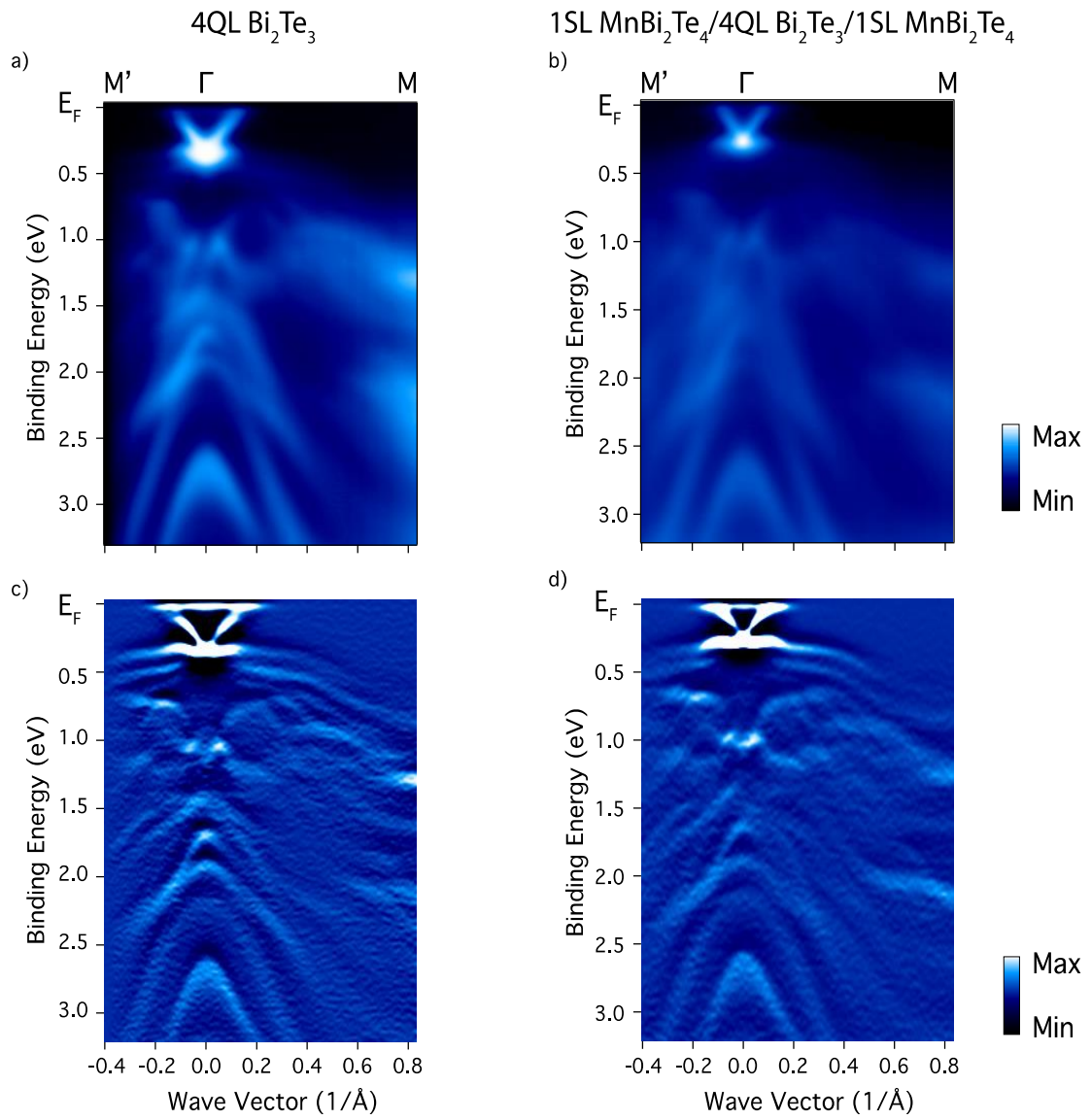


Figure S4 Valence band scan of a) 4QL BT, b) 1SL MBT/ 4QL BT/ 1SL MBT and second derivative enhanced spectra c) and d) taken at 54eV photon energy under P-polarisation. The bands of the heterostructure at high binding energy resemble that of 4QL BT.

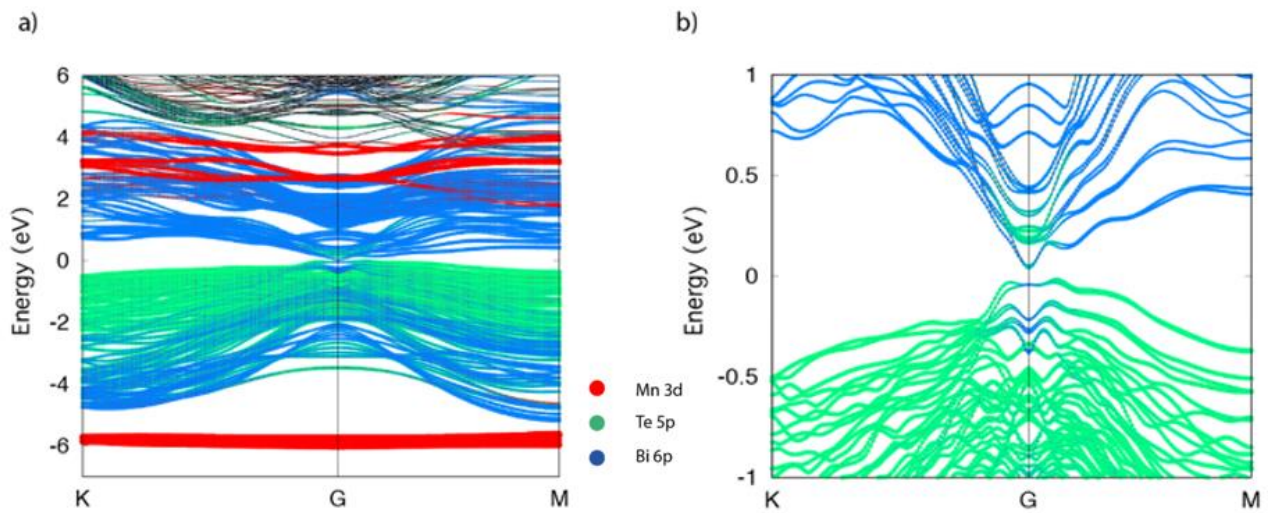


Figure S5 Atom orbital decomposed band structure along K- Γ -M Directions. a) the overview of the band structure where Mn 3d orbitals are represented in red solid circles, Te 5p in green and Bi 6p in blue. b) band structure near the gap region taken from a). Near Γ point, the states consist of mixing of Bi 6p and Te 5p state. The Mn d bands are far below and above the band gap region and there is very little p-d hybridisation near the gap.

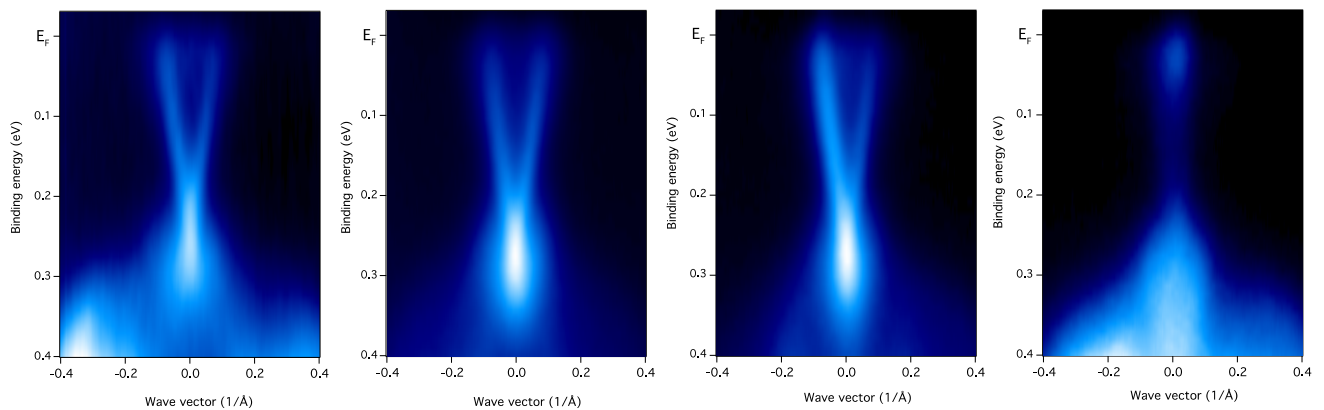


Figure S6 Band structure showing Dirac bands near Fermi level taken at different photon energies: a) 40 eV, b) 50 eV, c) 60 eV, d) 70 eV) with P-polarised light along Γ M direction. Dirac bands produce stronger signal at lower photon energy. At photon energy below 50 eV, the hole band top shows much weaker intensity.

